

METALLICITY EVOLUTION OF THE SIX MOST LUMINOUS M31 DWARF SATELLITES

NHUNG HO¹, MARLA GEHA¹, ERIK J. TOLLERUD^{1,3}, ROBERT ZINN¹, PURAGRA GUHATHAKURTA², AND LUIS C. VARGAS¹

¹ Astronomy Department, Yale University, New Haven, CT 06520, USA; ngocnhung.ho@yale.edu, marla.geha@yale.edu

² UCO/Lick Observatory, University of California, Santa Cruz, 1156 High Street, Santa Cruz, CA 95064, USA

Received 2013 September 22; accepted 2014 October 7; published 2014 December 24

ABSTRACT

We present global metallicity properties, metallicity distribution functions (MDFs), and radial metallicity profiles for the six most luminous M31 dwarf galaxy satellites: M32, NGC 205, NGC 185, NGC 147, Andromeda VII, and Andromeda II. The results presented are the first spectroscopic MDFs for dwarf systems surrounding a host galaxy other than the Milky Way (MW). Our sample consists of individual metallicity measurements for 1243 red giant branch member stars spread across these six systems. We determine metallicities based on the strength of the Ca II triplet lines using the empirical calibration of Carrera et al., which is calibrated over the metallicity range $-4 < [\text{Fe}/\text{H}] < +0.5$. We find that these M31 satellites lie on the same luminosity–metallicity relationship as the MW dwarf satellites. We do not find a trend between the internal metallicity spread and galaxy luminosity, contrary to previous studies. The MDF widths of And II and And VII are similar to the MW dwarf spheroidal (dSph) satellites of comparable luminosity; however, our four brightest M31 dwarf satellites are more luminous than any of the MW dSphs and have broader MDFs. The MDFs of our six M31 dwarf satellites are consistent with the leaky box model of chemical evolution, although our metallicity errors allow a wide range of evolution models. We find a significant radial gradient in metallicity in only two of our six systems, NGC 185 and Andromeda II, and flat radial metallicity gradients in the rest of our sample with no observed correlation between rotational support and radial metallicity gradients. Although the average properties and radial trends of the M31 dwarf galaxies agree with their MW counterparts at similar luminosity, the detailed MDFs are different, particularly at the metal-rich end.

Key words: galaxies: abundances – galaxies: dwarf – galaxies: individual (M32, NGC 205, NGC 185, NGC 147, And VII, And II) – Local Group

Supporting material: machine-readable table

1. INTRODUCTION

The increasing number of spectroscopic observations of individual stars available in nearby Milky Way (MW) dwarf galaxies allows for the detailed characterization of both the kinematic and metallicity distributions in these low-luminosity systems (Tolstoy et al. 2004; Helmi et al. 2006; Walker et al. 2007; Simon & Geha 2007; Battaglia et al. 2011; Kirby et al. 2011b; Simon et al. 2011). While kinematics provide a snapshot of the current dynamical state of a galaxy, the evolutionary history of a galaxy is encoded in its metallicity. More specifically, the distribution of metallicity within a galaxy hold clues to its star formation, gas accretion, and gas expulsion history (e.g., Prantzos & Silk 1998; Matteucci 2001; Lanfranchi & Matteucci 2004).

Deep photometric observations and chemical abundance studies of individual stars in many MW satellites have allowed for the detailed study of the formation histories of these systems (e.g., Aaronson & Mould 1985; Buonanno et al. 1985; Smecker-Hane et al. 1994; Stetson et al. 1998). For example, in two of the more massive MW dwarf satellites, Sculptor and Fornax, detailed chemical abundances have been determined for a significant portion of the red giant branch (RGB) stars in both galaxies (Tolstoy et al. 2004; Pont et al. 2004; Gullieuszik et al. 2007; Battaglia et al. 2008; Kirby et al. 2009; Starkenburg et al. 2010). Combining these abundances with deep photometric observations of their stellar populations allows for the deduction of their complete star-formation histories (SFHs; de Boer et al.

2012b; Coleman & de Jong 2008; de Boer et al. 2012a). However, detailed photometric and spectroscopic work is time intensive, and only recently has the wider MW dwarf population been observed in such detail (Dolphin et al. 2005; Holtzman et al. 2006; Brown et al. 2012; Gilmore et al. 2013).

The shapes of spectroscopic metallicity distribution functions (MDFs) for MW dwarf galaxies, along with age estimates of their constituent stellar populations, demonstrate that these objects have a wide range of SFHs (Gallart et al. 1999; Aparicio et al. 2001; Tolstoy et al. 2004; Helmi et al. 2006; Battaglia et al. 2011). Despite variations in individual SFHs, the MW dwarf galaxy satellites show a tight, linear luminosity–metallicity relation over more than three orders of magnitude in luminosity (Caldwell et al. 1992; Kirby et al. 2008b; McConnachie 2012). The trend between galaxy luminosity and galaxy metallicity also extends to more massive galaxies, with a flattening for the most massive objects (Skillman et al. 1989; Tremonti et al. 2004; Andrews & Martini 2013). A comparison to chemical evolution models further suggests that significant gas outflows are needed to explain the metallicities of most, though not all, of the MW dwarf galaxies (e.g., Tolstoy et al. 2001; Winnick 2003; Koch et al. 2006; Kirby et al. 2011b).

Dwarf galaxies around the Andromeda (M31) galaxy are sufficiently nearby to resolve individual stars, providing a second satellite system in which MDFs can be determined. M31 is host to a larger number of luminous satellites than the MW (13 M31 satellites versus seven M satellites brighter than $M_V = -10$), likely because of the larger total galaxy mass of the M31 system (Watkins et al. 2010; Yniguez et al. 2013). The M31 satellites appear to follow the same relationship

³ Hubble Fellow.

between luminosity and average metallicity as seen for the MW dwarf galaxies from both photometric and spectroscopic metallicity measurements (Caldwell et al. 1992; Kalirai et al. 2010; McConnachie 2012; Collins et al. 2013). While several studies have presented average metallicities (Kalirai et al. 2010; Collins et al. 2013) and in some cases binned radial metallicity profiles (Geha et al. 2010), none determined the spectroscopic MDFs for M31 satellites.

Characterizing the MDF of a galaxy requires individual metallicity measurements for a large sample of individual stars. High-resolution spectroscopy, the gold standard for determining stellar chemical abundances, is far too expensive to build up significant metallicity samples in systems beyond a few tens of kiloparsecs (e.g., Shetrone et al. 2003; Frebel et al. 2010). While early large spectroscopic metallicity data sets of globular clusters concentrated on integrated light measurements (e.g., Zinn & West 1984; Armandroff & Zinn 1988), the first large, homogeneous spectroscopic metallicity determinations of individual stars were carried out by Armandroff & Da Costa (1991) and Olszewski et al. (1991) using an empirical calibration between the strength of the Ca II triplet (CaT) line and [Fe/H]. This empirical calibration fails at the low-metallicity end where the Ca II lines are much narrower and non-LTE effects begin to dominate in the stellar photosphere (Gray 2005). Starkenburg et al. (2010) updated the CaT calibration, allowing for a nonlinear relationship between the CaT equivalent widths (EWs) over the metallicity range $-4.0 < [\text{Fe}/\text{H}] < -0.5$, basing the calibration on synthetic stellar spectra. However, this still does not fully cover the range of metallicities observed in the dwarf satellites and relies on synthetic spectra, which cannot fully capture the complex physics involved. Carrera et al. (2013, hereafter C13) has recently expanded the empirical calibration of the CaT by combining calibration data from metal-rich open clusters and extremely metal-poor halo stars to cover the range $-4.0 < [\text{Fe}/\text{H}] < +0.5$.

Here we present the MDF based on Carrera et al. (2013) calibrated Ca II triplet lines for the six brightest dwarf satellites around M31. These are the first MDFs presented for any satellite of M31. The data were taken homogeneously, using the Keck/DEIMOS spectrograph, and have been previously used to study the kinematics in these systems: M32 by Howley et al. (2013), NGC 205 by Geha et al. (2006), NGC 147 and NGC 185 by Geha et al. (2010), Andromeda II (And II) by Kalirai et al. (2010); Ho et al. (2012), and Andromeda VII (And VII) by Tollerud et al. (2012). M32, And II, and And VII are all part of the Spectroscopic and Photometric Landscape of Andromeda's Stellar Halo Survey.

The paper is organized as follows. We describe the spectroscopic data sets and membership selection process in Section 2. In Section 3, we describe in detail the CaT calibration used to determine [Fe/H] for stars in our sample. We next discuss the resulting metallicity distributions for M31 satellites, including average global metallicities (Section 4.1), global metallicity dispersions (Section 4.2), the MDFs and a comparison to a simple chemical evolution model (Section 4.3), and radial metallicity profiles (Section 4.4).

2. SPECTROSCOPIC OBSERVATIONS AND MEMBERSHIP SELECTION

We present individual stellar metallicities for the six brightest M31 dwarf galaxy satellites based on the strength of the calcium triplet lines near 8550 Å. Our data were taken using the Keck II 10 m telescope and the DEIMOS spectrograph

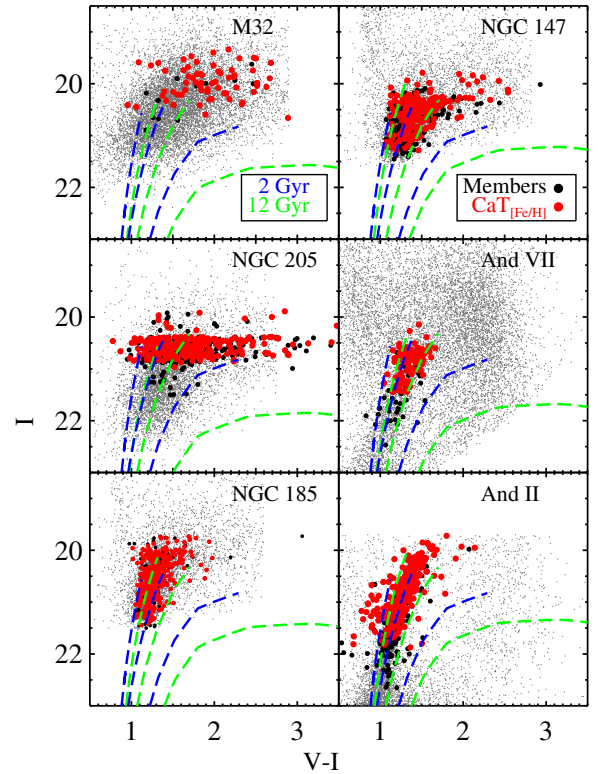


Figure 1. Color-magnitude diagram for the six most luminous M31 dwarf galaxy satellites, showing all photometric data (gray circles), member stars (filled black circles), and member stars with measured calcium triplet metallicity (filled red circles). Overlaid are 2 Gyr (blue dashed line) and 12 Gyr (green dashed line) Padova isochrones (Girardi et al. 2002) with $[\text{Fe}/\text{H}] = -2.0$, $[\text{Fe}/\text{H}] = -1.0$, and $[\text{Fe}/\text{H}] = 0.0$, respectively.

(Faber et al. 2003) with the 1200 line mm^{-1} grating covering a wavelength region 6400–9100 Å. The spectral dispersion was $0.33 \text{ Å pixel}^{-1}$, equivalent to $R = 6000$ for our $0''.7$ wide slitlets, or a FWHM of 1.37 Å . The spatial scale was $0''.12 \text{ pixel}^{-1}$. We refer the reader to Geha et al. (2010); Tollerud et al. (2012) and Howley et al. (2013) for details on the data reduction.

All spectra from the six M31 dwarf galaxies in our sample are sourced from previously published work with the partial exception of And VII. In all cases, the published work focused on kinematics derived from the Keck/DEIMOS spectra rather than metallicities. We summarize relevant targeting and membership details below and describe our new And VII data in Section 2.1.

Target selection for NGC 205, NGC 147, and NGC 185 was based on *R*-band and *I*-band photometry from the CFHT12K imager. Target selection for And II and And VII was based on imaging from the Kitt Peak Mosaic camera in the Washington System *M* and *T*₂ filters, as well as the *DDO51* intermediate-band filters centered near the surface-gravity-dependent Mgb and MgH absorption lines, which allow us to separate foreground MW dwarf stars and target M31 giant stars (Ostheimer 2003). Target selection was based on a star's position on the color-magnitude diagram (CMD) relative to a metal-poor 13 Gyr isochrone (Girardi et al. 2002) and position on the *M*–*DDO51* and *M*–*T*₂ color-color diagram (Tollerud et al. 2012). As seen in Figure 1, the targets cover a good fraction of the RGB.

We have used the memberships as determined by each of the galaxy source papers: for M32 in Howley et al. (2013), NGC 205 in Geha et al. (2006), NGC 147 and NGC 185 in Geha et al. (2010), And II in Ho et al. (2012), and Tollerud

et al. (2012) plus Section 2.1 for And VII. Five of our galaxies, NGC 205, NGC 147, NGC 185, And II, and And VII, each contain >100 member stars, and M32 contains over 60 member stars, all having spectra with an average per-pixel signal-to-noise ratio (S/N) of 6.0. The general method used for determining membership in these dwarf galaxies relies on the combined criteria of velocity, position in CMD space, and gravity-sensitive line indicators. While most of our dwarf galaxies have radial velocities that place them outside of the stellar velocity peaks of M31 and the MW, they still overlap with the wings of both distributions. In order to establish membership, a combination of three criteria was used: line-of-sight velocity to establish membership within the dwarf, strength of the Na I absorption line at $\lambda 8190 \text{ \AA}$ to remove foreground dwarf stars from the sample, and the distance to a fiducial isochrone to remove additional contamination. Details on the final sample used in our spectroscopic metallicity analysis can be found in Section 3.1.

2.1. Keck/DEIMOS Observations for And VII

Tollerud et al. (2012) presented 136 members for And VII based on two Keck/DEIMOS masks. We supplement these data with an additional two DEIMOS masks observed between 2012 September 15–17. The target selection and data reduction, as well as the probabilistic membership determinations, mirror that of Tollerud et al. (2012). Overall, we identify a total of 70 new RGB members in And VII, a significant increase from the previous sample. Our final And VII sample consists of 206 member stars.

3. CALCIUM TRIPLET METALLICITY CALIBRATION

To determine the metallicity ($[\text{Fe}/\text{H}]$) for individual stars across our sample, we utilize the near-infrared calcium CaT lines, which are an effective proxy for measuring the $[\text{Fe}/\text{H}]$ of RGB stars across a wide span of stellar ages (Pont et al. 2004; Cole et al. 2004; Carrera et al. 2007; Saviane et al. 2012). We measure EWs for the CaT lines and utilize the C13 metallicity calibration to convert the observed CaT EWs and I -band luminosity of RGB stars to $[\text{Fe}/\text{H}]$.

To measure the EW of the CaT lines, previous works have either directly integrated the continuum-subtracted flux or have fit the CaT lines with an analytic function and then integrated over the area of the resulting fit. A typical analytic function used to fit these lines is the Gaussian; however, as noted by previous authors (Rutledge et al. 1997; Cole et al. 2004; Carrera et al. 2007), the Gaussian profile is a poor fit to the CaT line shapes as metallicity increases because of the broadening at the wings of the line. To correctly measure the line shape, Cole et al. (2004), Carrera et al. (2007), and Saviane et al. (2012) showed that a sum of a Gaussian plus Lorentzian (G+L) provides a much better fit at both low metallicity, where line profiles have a more Gaussian shape, and high metallicity, where the profiles are more Lorentzian.

While the G+L function provides the best approximation to the shape of the true line profile for high S/N data ($\text{S/N} \geq 25 \text{ pixel}^{-1}$), stars within our sample have lower typical S/N ($<10 \text{ pixel}^{-1}$). The G+L profile is less stable at low S/N because the effects of imperfect sky subtraction creates artificial depressions, or enhancements, in the outer wings of the third Ca line at 8662 \AA . This effect is apparent when comparing the trend between EW_{8542} and EW_{8662} , where we did not observe a linear relation between the two lines as in C13. To mitigate this effect, we limit our fit to a pure Gaussian, which has a sharper boundary

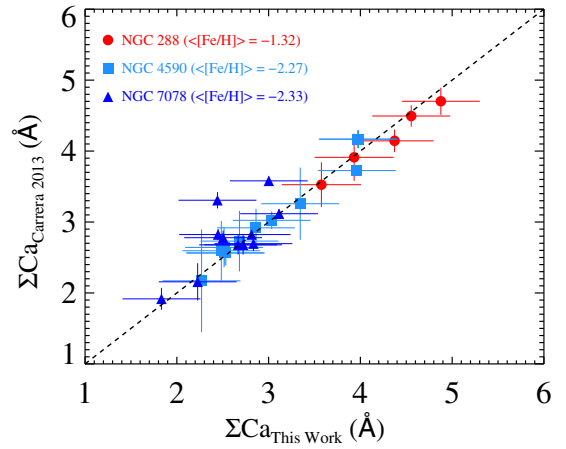


Figure 2. Comparison between the equivalent-width calculation for the CaT lines at 8542 \AA plus 8662 \AA using our transformed Gaussian profile fits and that of the globular cluster sample in Carrera et al. (2013) for three overlapping globular clusters. The dashed black line corresponds to a 1:1 relation between our measurements and that of C13. Despite the differences in continuum, bandpass, and functional form used to fit the EWs of the CaT lines, we are measuring the same quantities as C13.

at the wings and thus is more robust against instrumental wing dampening due to the presence of errant pixels.

Despite using a Gaussian to fit the line profiles, we still recover the true EWs of the lines by utilizing a linear relation between the EWs measured using a pure Gaussian and that using a G+L profile (Cole et al. 2004; Carrera et al. 2007; Saviane et al. 2012). To determine this relation, we used a sample of 22 globular clusters observed with DEIMOS from Kirby et al. (2008a), with a combined 429 RGB members and a minimum $\text{S/N} = 25$ per pixel, and we calculated the EWs for each of the two CaT lines using the same continuum and line definitions from Armandroff & Da Costa (1991) for both the Gaussian and G+L profiles. We find, by imposing passage through the origin (0,0), that $\text{EW}_{\text{G+L}} = 1.114(\pm 0.01) \times \text{EW}_{\text{G}}$, which is similar to the relation found by Saviane et al. (2012). Using this relation, we transformed our Gaussian EW measurements into G+L EW measurements.

To ensure that our EW measurements are correct with the inclusion of the correction factor from Gaussian to G+L, we compare our line measurements against that of C13, who used a G+L for their profile measurements, for three overlapping globular clusters, NGC 288, NGC 4590, and NGC 7078, with a total of 29 overlapping RGB stars. As shown in Figure 2, we find that our measurements, with the correction factor applied, are consistent with that measured by C13. Having verified that despite the differences in continuum and line bandpass definitions, we are measuring the same quantities as C13, we can now apply their calibration to our M31 dwarf RGB sample.

We use the line and continuum regions defined by Armandroff & Da Costa (1991) for the CaT lines at 8542 \AA and 8662 \AA . While the bandpass region used in our work is different from that of C13, we determined that this does not affect the recovered metallicity of the sample stars. We exclude the weakest line ($\lambda = 8498 \text{ \AA}$) from this work because of the aforementioned low S/N of our data; including the weakest CaT line introduces more noise than signal into the total EW. Adopting the C13 method, we determine the unweighted sum of the two lines as the total EW:

$$\Sigma\text{Ca} = \text{EW}_{8542} + \text{EW}_{8662}. \quad (1)$$

In addition to the combined EW, ΣCa , conversion to $[\text{Fe}/\text{H}]$ also depends on the luminosity of the individual star. The most widely used luminosity indicator is a star's magnitude above the horizontal branch (HB), $V - V_{\text{HB}}$. This luminosity indicator is used because the relationship between ΣCa and magnitude above the HB is very close to linear for isometallicity tracks. Thus, by accounting for this linear relationship in magnitude space, the relation between $[\text{Fe}/\text{H}]$ and ΣCa becomes linear and can be used to directly infer the intrinsic metallicity of a star. Because of the large distances from our dwarf galaxies, many do not have a well-determined HB magnitude. The distance estimates, determined via the tip of the RGB, may have large errors for some of these galaxies, but this error is dwarfed by the error in V_{HB} . The error in V_{HB} may be as high as 0.5 mag, resulting in a 0.1 dex error in the $[\text{Fe}/\text{H}]$ measurement. We instead utilize the absolute I -band magnitude, which has been shown to be more robust against age effects (Carrera et al. 2007) and has an overall smaller error attached to its determination for our sample.

We determine $[\text{Fe}/\text{H}]$ values for individual stars by combining the EW and absolute I -band magnitude of RGB stars using a two-line calibration to accommodate the lower average S/N of our data, from the C13 data set kindly provided by R. Carrera (2013, private communication):

$$[\text{Fe}/\text{H}] = -3.51 + 0.12 \times M_I + 0.57 \times \Sigma\text{Ca} - 0.17 \times \Sigma\text{Ca}^{-1.5} + 0.02 \times \Sigma\text{Ca} \times M_I, \quad (2)$$

where ΣCa is the total equivalent width of the measured Ca II lines, and M_I is the absolute I -band magnitude. This calibration utilizes a sample of 422 stars in globular and open clusters as well as field stars. It extends the CaT method to encompass the metallicity range $-4.0 < [\text{Fe}/\text{H}] < +0.50$ and over five orders of magnitude, starting from the HB and extending up to the tip of the rRGB.

We determine the errors in ΣCa by using 1000 Monte Carlo resamplings of each individual spectra with Gaussian random noise added to each pixel. The formal 1σ error is the square root of the variance about the mean of these 1000 realizations per star, for each of the two CaT lines. We add in quadrature to these errors a systematic error of 0.25 \AA calculated from repeat observations of 46 stars using the method outlined in Simon & Geha (2007) and Willman et al. (2011). These errors are then appropriately propagated to the $[\text{Fe}/\text{H}]$ calculations.

3.1. Metallicity Sample Selection Criteria

Membership for the majority of our RGB stars was sourced from earlier publications (Section 2). These member samples were selected for kinematic work, which has less stringent requirements on S/N and wavelength coverage than the present analysis. We therefore impose additional criteria on the published samples.

We first remove member stars that do not have spectral coverage in the rest-frame continuum and line bandpasses of the CaT. We next remove all stars with a continuum S/N $< 3 \text{ pixel}^{-1}$ because the EW measurements are unreliable below this S/N threshold. We motivate this S/N criteria by modeling our ability to recover the true EW by adding noise to a series of model spectra. We found that at a S/N $\sim 3 \text{ pixel}^{-1}$, the true EWs of the model spectrum could not be recovered within an error of 30%. To remove spectra with particularly bad sky subtraction, we impose a final criterion based on the reduced- χ^2 fit of the Gaussian profile fit to the spectrum. Of the stars removed by the

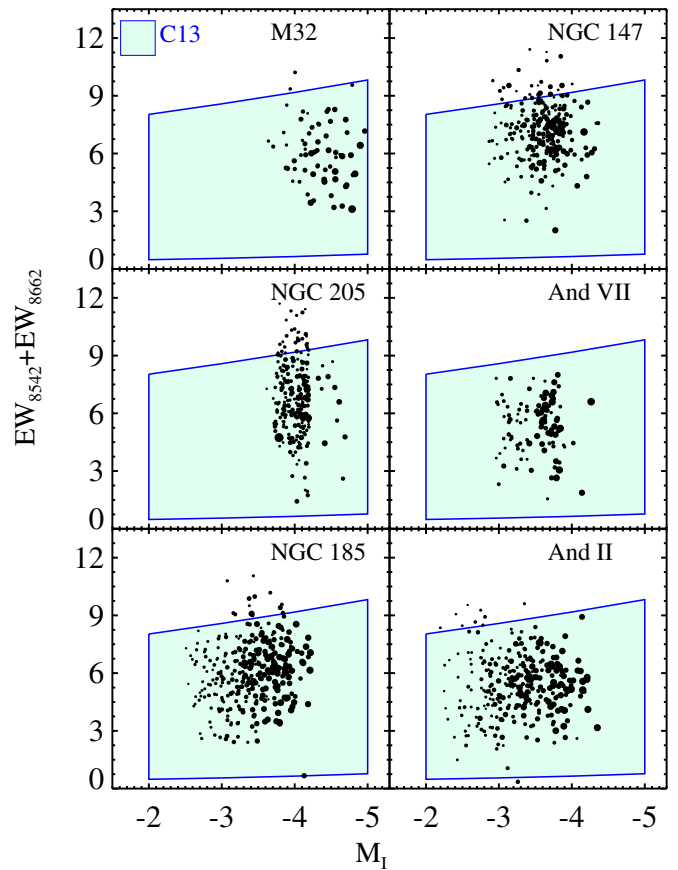


Figure 3. Total CaT EW as a function of absolute I -band magnitude, M_I , for member stars with a measured calcium triplet metallicity. Overlaid in light blue are the regions encompassed by the Carrera et al. (2013) calibration. Symbol sizes correspond to the S/N of the individual star such that larger symbols represent stars with larger S/N and smaller symbols correspond to stars with lower S/N.

above cuts, 181 were removed because of incomplete spectral coverage, 478 by too-low S/N, and 174 because of poor sky subtraction in the CaT region.

In Figure 3, we plot the region encompassed by the C13 calibration as function of the total EW (ΣCa) versus absolute I -band magnitude. We place our sample stars on this plot by converting the reddening-corrected, apparent I -band magnitudes into absolute magnitudes using the distances listed in Table 1. Out of the original 2,162 kinematic members, we measure a CaT EW for 1329 stars that pass the above quality cuts. Our final sample consists of 1243 stars that lie within the bounds of the calibration, shown in blue in Figure 3. Stars outside of the calibration bounds tend to have larger errors on their EW measurements and represent a small portion of the overall sample. For completeness, we include the C13 $[\text{Fe}/\text{H}]$ values of stars outside the calibration window in subsequent figures, but we do not include them in our average properties, MDF, or radial profile analysis. In Figure 4 we show the spectra for four stars in NGC 147 with similar M_I ranging from $[\text{Fe}/\text{H}] = +0.47$ to $[\text{Fe}/\text{H}] = -1.6$ and with S/N $\sim 6 \text{ pixel}^{-1}$, similar to the average S/N of the NGC 147 sample. We provide in Table 2 the derived $[\text{Fe}/\text{H}]$ and associated error for the 1243 stars that have calibrated $[\text{Fe}/\text{H}]$.

Figure 1 shows the CMD position of these metallicity-member stars (red) overlaid on all member stars (black). For comparison, we show in gray the photometric sample that

Table 1
Summary of M31 Dwarf Metallicity Properties

Dwarf	Distance (kpc)	M_V	N_{star}	$\langle[\text{Fe}/\text{H}]\rangle$ (dex)	$\sigma_{[\text{Fe}/\text{H}]}$ (dex)	Skewness	Kurtosis	R_{half} (pc)	$d[\text{Fe}/\text{H}]/d(r/r_h)$ (dex)	p_{eff} Z_{\odot}
M32	805	-16.4	64	-1.11 ± 0.08	0.59 ± 0.08	0.003 ± 0.06	-0.70 ± 0.17	110	-0.03 ± 0.03	0.08 ± 0.003
NGC 205	824	-16.5	224	-0.87 ± 0.05	0.51 ± 0.06	-0.68 ± 0.03	0.52 ± 0.15	590	-0.02 ± 0.01	0.19 ± 0.004
NGC 185	676	-14.8	321	-0.98 ± 0.05	0.51 ± 0.04	-0.51 ± 0.04	0.27 ± 0.41	623	-0.20 ± 0.01	0.14 ± 0.002
NGC 147	617	-14.6	230	-0.51 ± 0.04	0.38 ± 0.06	-0.87 ± 0.04	1.33 ± 0.28	458	$+0.02 \pm 0.02$	0.47 ± 0.005
And VII	762	-12.6	104	-1.30 ± 0.07	0.52 ± 0.07	-0.41 ± 0.06	-0.10 ± 0.30	776	-0.11 ± 0.04	0.08 ± 0.002
And II	652	-12.4	300	-1.25 ± 0.05	0.49 ± 0.04	-0.15 ± 0.02	-0.21 ± 0.14	1176	-0.40 ± 0.02	0.07 ± 0.001

Notes. The columns are ordered as follows: (1) galaxy name, (2) distance to the galaxy, (3) absolute V -band magnitude from, (4) number of stars in the final metallicity sample, (5) average-weighted mean metallicity with associated errors, (6) internal metallicity dispersion, calculated by taking the second moment of the distribution and accounting for increased dispersion from observational errors, along with Monte Carlo errors, (7) the skew, or third moment, of the distribution with associated errors, (8) the excess kurtosis, or fourth moment minus three, of the distribution with errors, (9) half-light radius, (10) the radial metallicity gradient as a function of half-light radius with associated errors from a least-squares fit, and (11) the best-fit value of the stellar yield resulting from fitting the leaky box model to the MDF of each dwarf. Values from Columns (2), (3), and (9) were taken from McConnachie (2012).

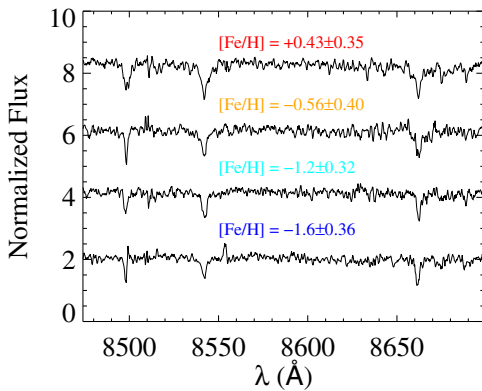


Figure 4. Normalized, boxcar-smoothed spectra, with a smoothing window of two pixels, centered around the CaT region for four stars in NGC 147 with similar absolute I -band luminosities, $M_I \sim -3.6$. These four stars have S/N values similar to the average S/N of all stars with a measured metallicity in NGC 147. The top spectrum is that of a star with a CaT $[\text{Fe}/\text{H}] = +0.43$, the second spectrum with a $[\text{Fe}/\text{H}] = -0.56$, the third spectrum with $[\text{Fe}/\text{H}] = -1.2$, and the bottom spectrum with $[\text{Fe}/\text{H}] = -1.6$. These spectra illustrate that as metallicity decreases, the strength of the CaT lines at 8542 Å and 8662 Å decreases as well.

the spectroscopic data were sourced from. Using previous photometric $[\text{Fe}/\text{H}]$ values for each of these objects, we show bounding 12 Gyr and 2 Gyr Padova (Girardi et al. 2002) isochrones of $[\text{Fe}/\text{H}] = -2.0$, $[\text{Fe}/\text{H}] = -1.0$, and $[\text{Fe}/\text{H}] = +0.00$.

To confirm that our CaT $[\text{Fe}/\text{H}]$ measurements using the C13 calibration are representative of the true $[\text{Fe}/\text{H}]$ of the individual RGB stars, we apply the same analysis and selection criteria to the eight dwarf spheroidal satellites (dSphs) from the K11 sample: Fornax, Leo I, Sculptor, Leo II, Sextans, Draco, Canes Venatici I, and Ursa Minor. The K11 sample uses spectral synthesis to determine metallicities, a more robust method with significantly more stringent S/N criteria. We calculate $[\text{Fe}/\text{H}]$ using our CaT method based on spectra kindly provided by E. Kirby (2013, private communication) and compare to the published K11 $[\text{Fe}/\text{H}]$ measurements, shown in Figure 5. We find consistent $[\text{Fe}/\text{H}]$ values for individual stars that are well within the measurement errors for all systems except Fornax. We find a discrepancy in Fornax in that we find many more metal-rich stars ($[\text{Fe}/\text{H}] > -0.5$) compared to that of K11. The K11 spectral synthesis grid does not extend more metal-rich than $[\text{Fe}/\text{H}] = 0.0$ and is calibrated to globular cluster stars only up to $[\text{Fe}/\text{H}] < -0.5$. This may be the source of discrepancy,

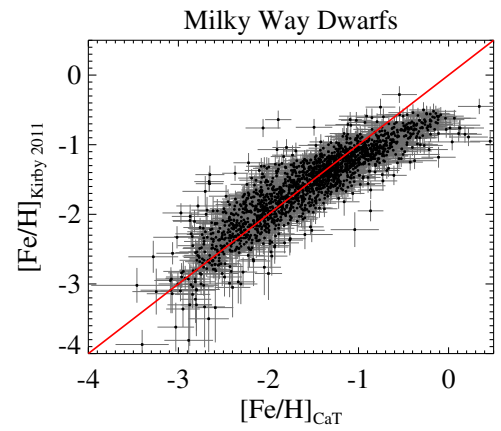


Figure 5. Comparison between $[\text{Fe}/\text{H}]$ values for 1993 individual RGB stars in MW dSphs using the methods detailed in this paper and $[\text{Fe}/\text{H}]$ values from K11's spectral synthesis method, along with the requisite errors for each star. The dSphs with metallicities shown here are Fornax, Leo I, Sculptor, Leo II, Sextans, Draco, Canes Venatici I, and Ursa Minor. The solid red line represents the 1:1 relation. At the low-metallicity end, there is a 1:1 relation between $[\text{Fe}/\text{H}]$ measured using the spectral synthesis technique and that using the CaT calibration from C13. At $[\text{Fe}/\text{H}] > -1.0$, the metallicities derived using the CaT begin to deviate from that of the spectral synthesis method. This flattening at higher metallicities shows that for the same stars, the CaT $[\text{Fe}/\text{H}]$ derived from the C13 calibration is higher than that derived using the spectral synthesis technique.

combined with possible differences in $[\alpha/\text{Fe}]$ between open cluster RGBs and globular cluster RGBs used in the C13 calibration.

We reproduce the $\langle[\text{Fe}/\text{H}]\rangle$, $\sigma([\text{Fe}/\text{H}])$, and the shape of the MDFs, as well as the radial trends reported for the K11 galaxies, using the C13 CaT calibration. In this paper, we highlight the results from our CaT calibration only for the three most luminous systems from the K11 sample, Fornax, Leo I, and Sculptor, because these have luminosities comparable to our six M31 dwarf galaxies.

3.1.1. Biases in Metallicity Distributions

To determine how representative our sample metallicities are of the true distribution of metallicity within each system, we investigate possible biases in our sampling. Incomplete or biased sampling of the true underlying metallicity of a galaxy could skew the shape of the MDF, the radial profile, and the observed average properties. These biases include incomplete sampling along the RGB track, insufficient S/N for a

metallicity subpopulation, preferentially selecting a metallicity subpopulation with color cuts, or incomplete spatial coverage of the galaxy.

For single-aged stellar populations, the metallicity of a star is correlated with its apparent magnitude, such that more metal-rich stars reside in the lower reaches of the RGB. Thus, because of observational limitations, metal-rich RGBs are usually also those with the lowest S/N compared to brighter, more metal-poor stars. Reitzel & Guhathakurta (2002) showed that by culling the stellar sample by magnitude, higher metallicity stars were preferentially removed because they were generally fainter and lie farther down in the RGB. Using a magnitude cutoff based on where the luminosity function of member stars turns over, we split the sample in two and compared the resulting MDFs. We find that stars below this threshold tend to contribute more metal-rich stars to the MDF than those above the turnover; however, the metallicity range covered by each respective sample remains the same. Similarly, to investigate the effects of S/N cuts, we divided the sample in half using an S/N such that there are approximately the same number of stars above and below this S/N sample bisector. We then compared the $\langle[\text{Fe}/\text{H}]\rangle$ and shape of the resulting MDF for the split sample and found no significant difference between their properties. This lack of difference between the split samples is because stars of all S/N lie along all positions in magnitude and color space because of variations in integration times between different masks, so we do not expect there to be a difference in metallicity space when cutting by S/N.

The spatial coverage for our sample is excellent for And II, And VII, NGC 147, and NGC 185, all of which have coverage over the full radial extent of the galaxy. For M32, the observations are limited to the outer edge of this galaxy ($>2r_{\text{eff}}$) because of the extremely high stellar density in the central region. Similar to M32, NGC 205 lacks coverage in the innermost regions because the high stellar density results in a lack of distinct sources. However, because it is not as compact as M32, we were able to probe within the effective radius. In these two cases, the spatial coverage exterior to these regions was excellent and well covers the observable area of the dwarf galaxies. For And VII, our sample represents the most spatially complete sample thus far, with coverage extending beyond two times the effective radius. For all of our galaxies, there are no strong spatial biases in the metallicity results because the spectroscopic data encompass an area equal to that of the photometric sample for each dwarf in which there were discrete sources.

Finally, our color selection for And II, And VII, NGC 147, and NGC 185 may introduce a metallicity bias into our sample. Metal-rich stars tend to have redder colors than more metal-poor stars for a single-aged stellar population, so any color selection on either the redward or blueward side could be removing a portion of either the metal-rich or metal-poor ends. While no color selection was imposed in NGC 205, we preferentially selected stars in all other systems in our sample to be near the best-fitting isochrone. Although no hard cut was imposed, redder stars were less likely to be observed. To determine this effect, we split our sample by the average metallicity in each system into “metal-rich” and “metal-poor” subsamples. We then examined the CMD position of these two metallicity subsamples, and, for all galaxies except NGC 185, we do not find a substantial difference in their properties using a two-dimensional Kolmogorov–Smirnov (K-S) test; all had p -values >0.01 . This shows that $[\text{Fe}/\text{H}]$ does not correlate with color, consistent with our sample containing many aged

stellar populations. For NGC 185, despite differences in the color distribution of metal-rich and metal-poor subsamples, the broadness of our color selection minimizes any preferential selection of a metallicity population. Given this, any bias that may have been introduced by color selection does not appear to have a large effect on our final metallicity distributions for the six dwarf galaxies.

4. RESULTS AND DISCUSSION

4.1. Global Metallicity Properties: Average $[\text{Fe}/\text{H}]$

For our six M31 dwarf galaxies, we determined the average metallicities and intrinsic metallicity dispersion. These are the first homogenous metallicity determinations of individual stars for three of our six M31 dwarf satellites: M32, NGC 205, and And VII. Previous works on determining the global metallicity properties for M31 dwarf satellites have relied on photometric metallicity estimates from isochrone fitting to the observed CMD (e.g., Kalirai et al. 2010) or coadded spectra of many stars (Collins et al. 2013). The errors associated with these methods are large, ranging from 0.1 to 0.7 dex (Collins et al. 2013), compared to measuring stellar metallicities star by star, and they fail to encapsulate the internal metallicity dispersion and distribution of these dwarf systems.

We determine the average metallicity for each galaxy using a weighted sum such that the weight is inversely proportional to the errors on the metallicity measurement. We find for M32 that the average metallicity of its outer regions is $\langle[\text{Fe}/\text{H}]\rangle = -1.11 \pm 0.09$. This agrees with the integrated spectroscopy metallicity measurements of Coelho et al. (2009) in the outer regions of M32; our observations do not cover the inner regions of M32, for which photometric metallicity estimates by Monachesi et al. (2011) suggest a more metal-rich ($\langle[\text{Fe}/\text{H}]\rangle = -0.20$) population. For NGC 205, the average metallicity of the entire population, including tidal tails, is $\langle[\text{Fe}/\text{H}]\rangle = -0.87 \pm 0.05$, consistent with the photometric metallicity estimates of $[\text{Fe}/\text{H}] = -0.8$ from McConnachie et al. (2005). Our CaT $\langle[\text{Fe}/\text{H}]\rangle$ measurements for NGC 147 and NGC 185 are more metal-rich at $\langle[\text{Fe}/\text{H}]\rangle = -0.51 \pm 0.04$ and $\langle[\text{Fe}/\text{H}]\rangle = -0.98 \pm 0.05$, respectively, compared to the $\langle[\text{Fe}/\text{H}]\rangle = -1.1 \pm 0.1$ and $\langle[\text{Fe}/\text{H}]\rangle = -1.3 \pm 0.1$ values found by Geha et al. (2010). This discrepancy is due in part to differences in measuring the CaT lines (Geha et al. use direct sums), as well as differences in the calibration: Geha et al. (2010) used the Rutledge calibration, which is linear across the entire $[\text{Fe}/\text{H}]$ regime, whereas the C13 calibration is nonlinear at both the metal-rich and metal-poor ends. The most recent $\langle[\text{Fe}/\text{H}]\rangle$ measurement for And VII was done using KECK/LRIS by Grebel & Guhathakurta (1999) with a reported $\langle[\text{Fe}/\text{H}]\rangle = -1.40$, consistent with our measured $\langle[\text{Fe}/\text{H}]\rangle = -1.30 \pm 0.07$. Finally, in Ho et al. (2012) the metallicity for And II utilized the Starkenburg calibration and direct integration of the line bandpass regions; they found an $\langle[\text{Fe}/\text{H}]\rangle = -1.39 \pm 0.03$. In this work we find an $\langle[\text{Fe}/\text{H}]\rangle = -1.25 \pm 0.05$, which is more metal-rich than their findings.

As a group, our six dwarf galaxies follow the metallicity–luminosity relation seen in the MW and M31 satellites (Kirby et al. 2011b, hereafter K11; McConnachie 2012; Collins et al. 2013). In Figure 6, top panel, we place our sample galaxies (filled red stars) on the metallicity–luminosity plane alongside all MW satellites with individual RGB star metallicity measurements (filled gray circles) and M31 satellites with coadded CaT metallicities (filled red triangles). Using the combined sample of

Table 2
Metallicity of Individual Stars in Each Galaxy

Star ID	Galaxy Name	R.A. (h : m : s)	Decl. (° : ' : ")	V-I	V	[Fe/H] dex	[Fe/H] _{error} dex
1	M32	0:42:48.50	40:47:24.20	1.6	21.36	-1.16	0.36
2	M32	0:42:45.10	40:48:05.40	1.6	21.64	-0.84	0.36
3	M32	0:42:52.30	40:48:53.20	2.2	22.08	-0.06	0.41
4	M32	0:42:47.05	40:49:34.40	1.5	21.66	-0.84	0.39
5	M32	0:42:41.79	40:49:36.80	2.0	21.81	-2.55	0.37
6	M32	0:42:52.50	40:49:37.50	2.1	22.48	-1.45	0.48
7	M32	0:42:56.27	40:49:38.10	2.6	22.69	-0.45	0.42
8	M32	0:42:41.63	40:49:46.00	1.8	21.64	-0.37	0.38
9	M32	0:42:38.25	40:50:56.60	1.3	21.54	-1.13	0.38
10	M32	0:42:51.25	40:51:07.90	3.6	23.34	-1.84	0.35
11	M32	0:42:47.46	40:51:09.70	1.6	21.15	-1.28	0.32
12	M32	0:42:44.16	40:52:56.60	1.9	21.38	-1.07	0.27
13	M32	0:42:34.43	40:53:04.70	1.7	21.19	-1.76	0.28
14	M32	0:42:46.72	40:54:13.60	1.4	21.15	-0.09	0.35
15	M32	0:42:46.62	40:48:01.50	2.4	22.63	-1.52	0.42
16	M32	0:42:52.74	40:50:41.90	1.9	22.24	-1.24	0.38
17	M32	0:42:34.13	40:50:43.70	1.8	21.84	-1.08	0.39
18	M32	0:42:47.34	40:52:55.40	1.4	21.74	-1.76	0.56
19	M32	0:42:40.30	40:53:52.80	1.6	21.36	-1.23	0.62
20	M32	0:42:45.63	40:54:24.00	1.8	21.82	-1.43	0.46
21	M32	0:42:51.69	40:48:37.80	1.9	21.96	-1.05	0.40
22	M32	0:42:43.88	40:49:26.20	1.8	21.68	-1.09	0.33
23	M32	0:42:42.70	40:50:23.00	1.9	21.63	-1.28	0.31
24	M32	0:42:35.25	40:50:34.70	2.4	21.97	-1.78	0.43
25	M32	0:42:44.80	40:50:45.70	1.7	21.60	-1.50	0.44
...
...

Notes. The columns are ordered as follows: (1) star ID, (2) host galaxy, (3) right ascension, (4) declination, (5) color, (6) extinction-corrected absolute V-band magnitude, (7) metallicity, and (8) metallicity error.

(This table is available in its entirety in machine-readable form.)

M31 satellites with coadded or individual spectroscopic metallicity measurements, we derive the following relation between luminosity and metallicity:

$$\langle [\text{Fe}/\text{H}] \rangle = (-1.94 \pm 0.09) + (0.33 \pm 0.05) \log \left(\frac{L_V}{10^5 L_\odot} \right). \quad (3)$$

The resulting relation using just M31 dwarf galaxies with spectroscopic measurements (dashed red line in Figure 6, top) is similar to the relation observed in K11 for just MW dSphs (dashed line in Figure 6, top). The linear Pearson coefficient for this combined sample is 0.87, showing that luminosity and $\langle [\text{Fe}/\text{H}] \rangle$ are highly correlated. This positive trend between galaxy luminosity and galaxy $\langle [\text{Fe}/\text{H}] \rangle$ has been shown to be linear for more massive galaxies, with a flattening for the most massive galaxies (Tremonti et al. 2004; Andrews & Martini 2013). The large range over which this relation holds suggests that mass is the key variable controlling the retention of a dwarf galaxy's gas. This is plausible because lower luminosity and by extension lower dark matter halo mass systems have shallower potential wells and are less efficient at retaining their metals in the presence of internal wind-driven outflows such as massive stellar or supernova winds.

4.2. Global Metallicity Properties: Internal Metallicity Dispersion

While in general the mass appears to regulate the retention of metal-rich gas in a galaxy, its relation to the details of the

star-formation process is still nebulous. To address this, we can look at the internal spread in metallicity, which gives clues to the timescale of star formation. K11 showed that the intrinsic spread in a galaxy's $[\text{Fe}/\text{H}]$ is anticorrelated with its luminosity for the MW dSphs in the sense that more massive systems have a smaller internal metallicity spread than do lower luminosity systems.

To determine whether our six M31 satellites obey this observed relation, we calculate the internal metallicity dispersion using the method described in K11. In K11, the metallicity dispersion is defined to be the second moment about the mean of the distribution, which allows us to describe a dispersion that is distribution independent. We perform a Monte Carlo bootstrap to determine the errors on the dispersion measurement using 1000 resamplings drawn from a normal distribution that is scaled to the metallicity error for each individual star. In order to fairly compare the samples, we reproduce the average metallicities and internal metallicity dispersions, as well as place error bars on the metallicity dispersion measurements, for the 14 galaxies from K11 used to construct this relation, as seen in Figure 6, bottom. Additionally, given the discrepancy in the derived metallicities for Fornax stars, we include both the K11 metallicity dispersion, $\sigma([\text{Fe}/\text{H}]) = 0.31$, as well as that from our work using the C13 calibration, $\sigma([\text{Fe}/\text{H}]) = 0.42 \pm 0.01$.

Adding to the results of Leaman et al. (2013), who found that the anticorrelation observed in K11 flattens out at higher luminosities, we find that the anticorrelation observed in K11 is completely removed for more luminous systems ($\gtrsim 10^5 L_\odot$), as

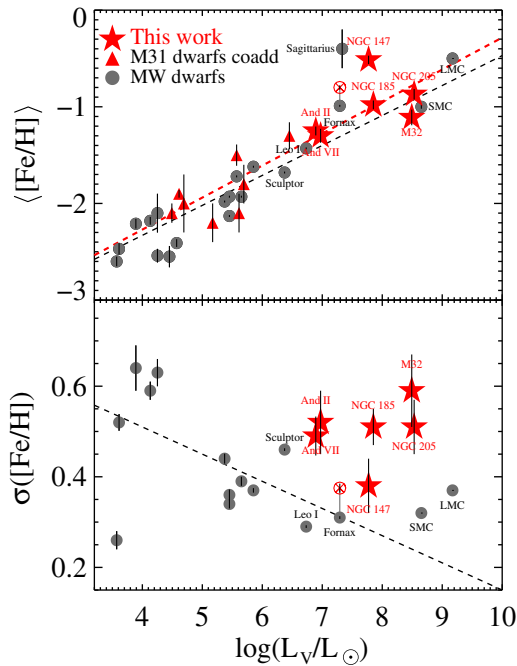


Figure 6. Top: average metallicity of Milky Way (black symbols) and M31 (red symbols) dwarf galaxies as a function of luminosity. Our six dwarf galaxies are shown as red stars, and red triangles are based on coadded spectra from Collins et al. (2013). This demonstrates that the M31 dwarf galaxies follow the same metallicity–luminosity relation as the MW dSphs. Bottom: metallicity dispersions as a function of luminosity. Contrary to the trend derived in K11 (dashed black line), we do not observe an anticorrelation between intrinsic metallicity dispersion and luminosity.

shown in Figure 6, bottom. For the combined sample we find a linear Pearson coefficient of -0.18 . This shows a weak correlation between internal metallicity spread and luminosity, in contrast to K11. The lack of relation between intrinsic metallicity dispersion and luminosity at higher luminosities may be explained by the different ways in which star formation occurs in lower mass galaxies compared to more massive systems. In lower mass galaxies, star formation is more stochastic because of these galaxies’ inability to retain metal-enhanced gas from outflow events such as supernova winds. For more massive systems, their deeper potential wells mean that they are more resilient against wind-driven outflow events. This ability to retain metal-enhanced gas means that star formation can proceed smoothly, compared to less massive systems.

4.3. Metallicity Distributions

The cumulative and differential metallicity distribution functions (CMDF and MDF, respectively) of a galaxy represent an admixture of its integrated SFH and its gas accretion or expulsion history. By fitting the shape of the metallicity distribution with a model of galactic chemical evolution, we can broadly quantify the gas dynamics associated with the SFH of the galaxy. For all of the galaxies in our sample, this work represents the first spectroscopically determined CMDF and MDF of a large number of stars in each galaxy.

We fit a simple chemical evolution model, the leaky box model (Tinsley 1980 and references therein), to the CMDFs of our six dwarf galaxies. In this model, the system starts from an initial gas reservoir with metallicity $[\text{Fe}/\text{H}]_0$ and is progressively self-enriched through instantaneous recycling and mixing of the by-products of the star-formation cycle. The primary model

parameter is the effective yield, p_{eff} , which is expressed as a fraction of the solar abundance. In the limit of no outflows, p_{eff} approaches the theoretical yield, p , for a stellar population. This is the closed-box regime. While no gas inflow is allowed into the system, a gas outflow with the same metallicity as the by-products of star formation (i.e., a homogeneous wind) acts to decrease the yield from its nucleosynthetic value p by removing gas that could otherwise enrich the interstellar medium (ISM). In this paper, we utilize the general, cumulative form:

$$N_{\star}(< [\text{Fe}/\text{H}]) = A \left[1 - \exp \left(\frac{10^{[\text{Fe}/\text{H}]_0} - 10^{[\text{Fe}/\text{H}]} }{p_{\text{eff}}} \right) \right], \quad (4)$$

where A is a normalization factor that accounts for the amount of metal-rich gas remaining in the system. In this work, we use the initial condition of a pristine gas, $[\text{Fe}/\text{H}]_0 < < [\text{Fe}/\text{H}]$, because our observational errors do not allow for a robust derivation of $[\text{Fe}/\text{H}]_0$.

We perform a Levenberg–Marquardt χ^2 minimization to find the best-fit leaky box model to our spectroscopic CMDFs. To determine whether each observed CMDF is consistent with its respective best-fit leaky box, we utilize a one-sided K-S test to compare the best-fit CMDF and the model. However, given that the model CMDFs are best-fit models to the data, the standard probabilities associated with the test statistic no longer apply because they are not distribution independent. Using the methods outlined in Feigelson & Jogesh Babu (2012), we determined the probability distribution for each galaxy and its best-fit leaky box model by utilizing a parametric bootstrap. For each galaxy, we construct cumulative distribution functions for both the model and the data. We then perform 1000 bootstrap resamples of the best-fit model and convolve each model with individual measurement errors drawn from the error distribution of each galaxy. Given that the best-fit model is error free, we construct the reference error-convolved, best-fit model by doing a running median of the 1000 error-convolved, bootstrapped model distributions. The K-S statistic, $D = \max |F_n(x) - F(x)|$, where $F(x)$ is the model and $F_n(x)$ is the bootstrap of the model, is calculated for each bootstrap resample. The final, ordered distribution of D for the 1000 bootstrapped samples represents the probability distribution of the null hypothesis. The resulting D statistic, D^* , between this reference model and the data is then used to tabulate a p_{KS} value. In this work, we use $p_{\text{KS}} = 0.01$ as the significance value below which the null hypothesis holds.

The resulting error-convolved, best-fit leaky box (blue) models are shown in Figure 7 along with the p_{eff} value for each model. Similar to previous MW studies, we find that the best-fit models have low $p_{\text{eff}} < 0.2$, except for NGC 147. While theoretical yields p are not known precisely owing to uncertainties in the initial mass function (IMF) and nucleosynthetic calculations, various studies report p values higher than our p_{eff} measurements, suggesting that the low p_{eff} values are evidence for significant gas outflows. For a wide range of assumed IMFs and metallicities of supernova progenitors, Maeder (1992) and Kobayashi et al. (2006) report theoretical yields of $p > 0.4$ (for Maeder 1992, we consider their models B, C, and D for two different IMF power-law exponents). Thus, the measured yields, $p_{\text{eff}} < 0.2$, are lower than these theoretical values. This inequality holds even after accounting for an overabundance in primary elements (e.g., O) relative to the measured Fe abundances, which is likely not higher than a factor of two, given the range of $[\alpha/\text{Fe}]$ enhancements in dwarf galaxies (e.g., Tolstoy et al. 2009; Kirby et al. 2011a; Vargas et al. 2014). The CMDFs of all six dwarf galaxies in our sample are consistent

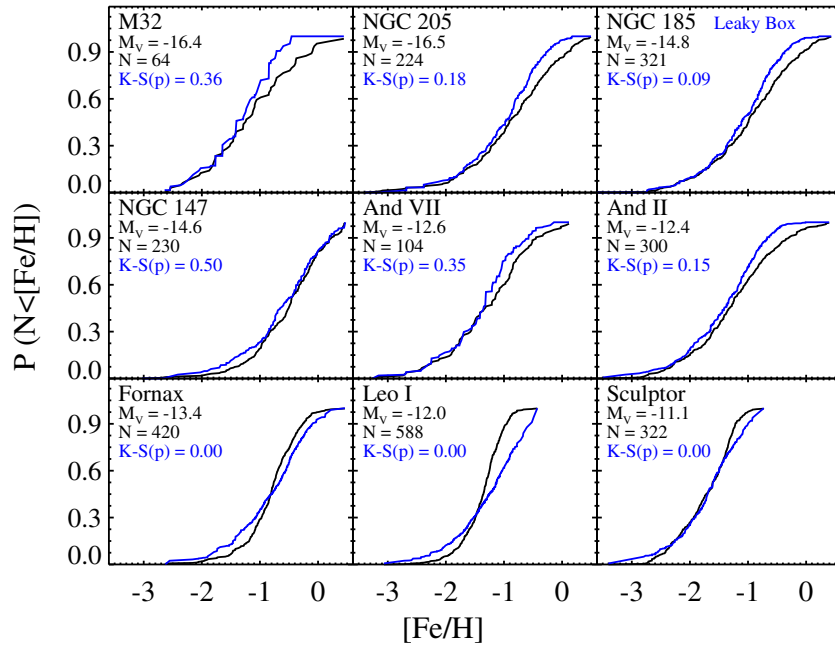


Figure 7. Cumulative metallicity distribution functions (CMDFs) for our six dwarf galaxies (top two rows), along with three MW dSphs (bottom row) with luminosities similar to And VII and And II, the two least luminous dwarf galaxies in our sample. Solid black lines represent the CMDFs of all stars within the bounds of the C13 calibration. The best-fit, Levenberg–Marquardt χ^2 -minimized, error-convolved leaky box (blue) models are presented. Using a one-sided K-S test, we determine the probability that our observed CMDFs are drawn from the leaky box chemical evolution models. For all six of our M31 dwarf satellites, we find that their observed CMDFs are consistent with being drawn from a leaky box distribution. Our MW dSph comparison sample of Fornax, Leo I, and Sculptor has K-S p values that are inconsistent with being drawn from a leaky box distribution, in accord with the results from K11. The resulting K-S p values for each of the nine dwarf galaxies are shown in the legend.

with being drawn from a pristine, leaky box CMDF with low values of p_{eff} . Because of the large observational errors in our sample, we are unable to robustly discern a difference between a pristine, leaky box and a pre-enriched, leaky box. We include the CMDFs of Fornax, Leo I, and Sculptor along with their best-fit leaky box models as a comparison sample. Consistent with K11, we find that neither Fornax, Leo I, or Sculptor have distributions consistent with a leaky box.

Despite the M31 satellite CMDFs showing consistency between the observed data and the leaky box model, there are inconsistencies that become more apparent when observing the shapes of the differential metallicity distribution (MDF). We show in Figure 8 the MDFs of our six dwarf galaxies and the three comparison MW dSphs along with the error-convolved, best-fit leaky box model. These MDFs show that similar to the MDFs of MW dSphs, there is diversity in the shapes of the distributions, from peaky as in NGC 147 to very symmetric in the case of And II. In order to further quantify the shapes of the MDFs, we calculate both the skewness (γ) and excess kurtosis (κ) for each of the six dwarf galaxies, as shown in Table 1. The skewness of a distribution gives insight into its symmetry, with negative values representing those distributions with longer metal-poor tails and positive values representing distributions with longer metal-rich tails. The excess kurtosis, defined as the fourth moment minus three, quantifies the peakiness of a distribution. Positive values indicate distributions that are more sharply peaked than a standard Gaussian, whereas those with negative values of excess kurtosis are broader than a standard Gaussian. In the following paragraphs, we will discuss in detail the shapes of the MDFs for each dwarf and compare them to previous photometric works.

M32. The MDF presented in this paper is the first spectroscopic MDF composed of individual stars from M32. Despite the sparse sampling limited to the outer regions of M32, the

MDF is broadly consistent with previous works at the same radial distance (Coelho et al. 2009). The width of the MDF is large, with a span of almost 3 dex, comparable to previous photometric work that shows similar broadness in the RGB population (Grillmair et al. 1996; Monachesi et al. 2011). The leaky box provides a consistent fit ($p_{\text{KS}} = 0.36$) with the CMDF of M32, with a best-fit effective yield of $p_{\text{eff}} = 0.08$. This consistency with a low p_{eff} leaky box model shows that gas outflows have played a role in the chemical evolution of M32’s outer regions.

NGC 205. The MDF of NGC 205 includes stars from both the main body of the galaxy and the tidal tails. Similar to Butler & Martínez-Delgado (2005), we observe a long, metal-poor tail ($\gamma = -0.68$) spanning over 1 dex in the MDF of this galaxy. The bulk of the RGB stars in NGC 205, however, form a symmetric, fairly narrow peak ($\kappa = 0.52$) around $\langle [\text{Fe}/\text{H}] \rangle = -0.87$ dex, similar to the position of the peak from the photometrically obtained MDF. The leaky box model provides a consistent fit ($p_{\text{KS}} = 0.18$) with a best-fit effective yield of $p_{\text{eff}} = 0.19$. However, upon further examination of the MDF, we can see that the number of metal-poor stars predicted by the leaky box model is higher than what is observed.

NGC 185. The MDF of NGC 185 is asymmetric and has a thick, metal-poor tail ($\gamma = -0.51$) along with a somewhat broader peak region ($\kappa = 0.27$) compared to NGC 205. This broad peak was also observed photometrically by Butler & Martínez-Delgado (2005), who showed that this broadness is a result of an extended SFH. The best-fit leaky box model has an effective yield of $p_{\text{eff}} = 0.14$. Similar to M32 and NGC 205, the leaky box model underpredicts the number of metal-rich stars. However, compared to NGC 205, the metal-rich side of the MDF of NGC 185 is much steeper. This steepness on the metal-rich side could possibly be due to strong galactic winds that drive out metal-enhanced gas, preventing further metal-rich star formation (Lanfranchi & Matteucci 2004).

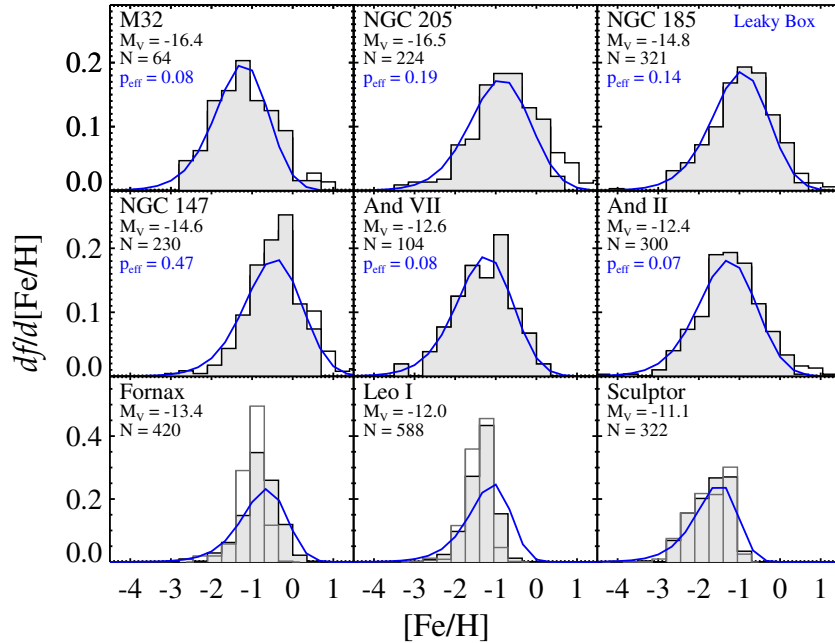


Figure 8. Normalized metallicity distribution functions (MDFs) of our six galaxies (top two rows) along with three MW dSphs (bottom row) with luminosities similar to And VII and And II, the two least luminous dwarf galaxies in our sample. In the top two rows, black-bordered, gray-filled histograms represent the metallicity distribution functions of all stars within the bounds of the C13 calibration, and the unfilled portions show those stars that lie outside the bounds of the calibration but have metallicities calculated using the C13 calibration. In the bottom row, gray-lined histograms represent the MDFs from the spectral synthesis method of Kirby et al. (2011b), and gray-filled histograms represent the CaT [Fe/H] measurements using the methods outlined in this paper. Overlaid solid blue lines are the error-convolved fits to the MDFs using a leaky box model. The average error in our [Fe/H] measurements is ≥ 0.4 dex, similar to the bin size of 0.35 dex.

NGC 147. The MDF of NGC 147 is highly asymmetric ($\gamma = -0.87$), with a narrow peak region ($\kappa = 1.33$), a long metal-poor tail, and a steep metal-rich cutoff. Sharp, narrow peaks (high κ) can be produced if the satellite were to accrete a significant amount of metal-poor (relative to the ISM) gas from the surrounding environment (Lynden-Bell 1975; Kirby et al. 2011b). A sharp peak may also be in part a reflection of the steep drop in the MDF on the metal-rich side, possibly due to strong galactic winds (Lanfranchi & Matteucci 2004). This steepness on the metal-rich side was also seen in photometric MDFs from Butler & Martínez-Delgado (2005); however, our MDF peaks are 0.3 dex higher than that from photometric works. The best-fit effective yield from the leaky box model is $p_{\text{eff}} = 0.47$, much higher than any other dwarf in the sample and thus not inconsistent with a range of possible theoretical yields. A possible explanation for the higher p_{eff} (higher average [Fe/H]) for NGC 147 compared to other galaxies at similar luminosity is the current tidal interaction between M31 and NGC 147 (Lewis et al. 2013; Ibata et al. 2013). Looking at the PAndAS maps from (Lewis et al. 2013; Ibata et al. 2013), we see that the tidal tails for NGC 147 are very extended and span a projected size that is more than four times more extended than our spectroscopic data. Additionally, these tails are composed of mostly metal-poor stars (Ibata et al. 2013), whereas the central regions of the galaxy are mostly metal-rich. While we cannot state how much mass is present in these extended tidal tails because that data has not been published, our observations of a higher-than-expected average [Fe/H] for NGC 147 can be explained by this tidal disturbance.

And VII. Very little work has been done on either the photometric or spectroscopic metallicity of And VII other than to determine its $\langle [\text{Fe}/\text{H}] \rangle$. The MDF of And VII is broad ($\kappa = -0.10$) with an ill-defined peak in its MDF, and it is more symmetric ($\gamma = -0.41$) than the NGC dwarf satellites of M31.

Its MDF is most similar to that of Canes Venatici I, which was found by K11 to have an MDF consistent with being drawn from a leaky box model. The leaky box model provides a consistent fit to both the metal-poor and metal-rich slopes of And VII, with a best-fit effective yield of $p_{\text{eff}} = 0.08$.

And II. The MDF of And II is fairly symmetric ($\gamma = -0.15$) with both a thick peak region ($\kappa = -0.21$) and both metal-rich and metal-poor tails, consistent in shape with the photometric MDFs from McConnachie et al. (2007) and Kalirai et al. (2010). The leaky box model provides a good fit to both the metal-poor and metal-rich slopes with a best-fit effective yield of $p_{\text{eff}} = 0.07$, and II's SFH appears to be extended with both old and intermediate-aged populations in the HB (McConnachie et al. 2007). This extended period of star formation could account for the broadness of the peak region, and weaker galactic winds could account for the shallower metal-rich slope.

Steepness on the metal-rich side of the shape of the MDF implies strong mass loss resulting in a sudden cessation of star formation. The metal-rich gas that would have later formed into metal-rich stars was removed from the system by either environmental effects between the dwarf and its host halo environment or internal effects from the process of star formation. Environmental effects, such as ram pressure or tidal stripping due to the interaction between a dwarf and its host halo, could remove gas from the system and halt further star formation (Gunn & Gott 1972; Faber & Lin 1983; Piatek & Pryor 1995; Gnedin et al. 1999). Even if individually these environmental effects are inefficient at gas removal, Mayer et al. (2006) and Łokas et al. (2010) showed that a combination of ram pressure stripping and tidal shock heating is very efficient at gas removal. Internal effects that could remove gas and inject energy into the dwarf's ISM are mainly wind driven, either by massive stars or supernovae (Larson 1974). The potential wells of these dwarf galaxies are shallow enough that wind-driven outflows could drive out metal-

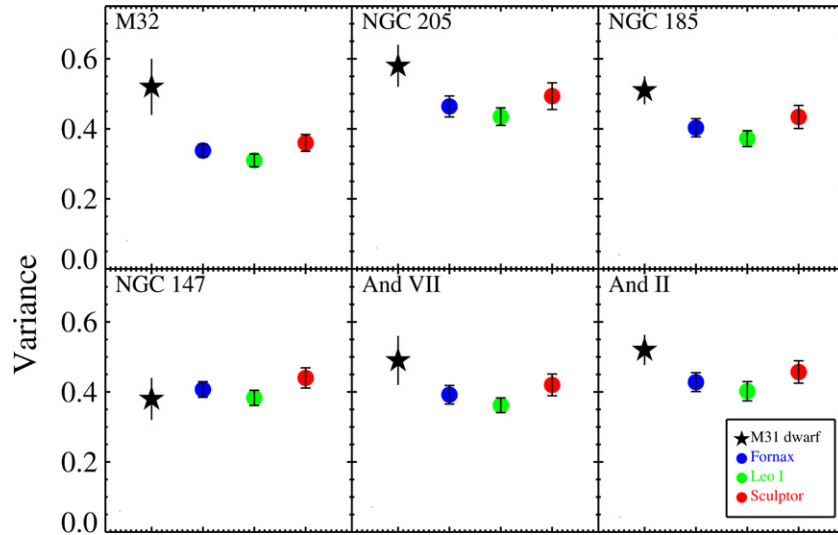


Figure 9. In each of the six panels, we show the second moment (variance) for each M31 dwarf satellite (black star) along with the error-convolved variance of Fornax (blue circle), Leo I (green circle), and Sculptor (red circle). We use the error distribution associated with each reference M31 satellite and convolved each MW dSph with 1000 bootstrap resamples from this error distribution. The values plotted here represent the mean variance of each 1000 bootstrap resample along with $1 - \sigma$ error bars calculated from the bootstrap. Even after convolving the MW dSph data with the larger M31 errors, we see that for five out of our six galaxies their metallicity spreads are still larger than that of the MW comparison sample. Thus, the broader MDFs observed in most of our dwarf satellites are an intrinsic property.

enhanced gas fairly quickly (Dekel & Silk 1986). However, H I observations of Local Group dwarf galaxies by Grcevich & Putman (2009) have shown that the gas content of a dwarf galaxy is more correlated with its distance to a host halo than to its total mass or stellar content. Thus, internal effects likely play a smaller role in halting star formation in local dwarf galaxies.

For most of our M31 satellites, the MDFs show broad distributions that are more symmetric than MW dSphs. To determine if this broadness is an intrinsic effect or is due to our larger observational error, we convolve stars in the three MW dSphs of comparable luminosity, Fornax, Leo I, and Sculptor, with the observational errors of stars from each dwarf satellite in our sample. We remove the observational error associated with each MW star by subtracting it in quadrature to a bootstrapped observational error sampled from the error distribution of each reference M31 satellite. We then compute the second moment (hereafter, variance), used to quantify the spread of the distribution, of these 1000 bootstraps. Using the mean value this distribution of second moments as the value that quantifies the error-convolved spread for each MW dSph, we compare it to the reference M31 satellite. We perform this method on all six galaxies in our sample, producing a unique error-convolved distribution of the three MW dSphs for each M31 satellite.

The variance for each convolved MW dSph is shown in Figure 9 for reference. For Leo I (green), in no case does the error-convolved variance become broader than the distribution of the reference M31 dwarf. In contrast, Sculptor, which is known to have an MDF with a large span due to an extended SFH, has error-convolved MDFs with a spread comparable to the M31 dwarf galaxies. For distributions that are intrinsically peaky, such as Leo I, the inclusion of larger observational errors will broaden out the distribution, but the intrinsic shape is mostly preserved. Likewise, distributions that are naturally broad, such as Sculptor, will only get broader, but again the intrinsic shape remains the same. For Fornax (blue in Figure 9), which is more luminous than And VII and And II, the spatial sampling of our data includes only the central regions (~ 1 core radius).

Battaglia et al. (2006) and Leaman et al. (2013) both used a much larger sample that extends out to 5 core radii and have shown that Fornax possesses a metallicity gradient, which we do not observe using our data. Thus, the variance value that we calculate is an underestimate of the true variance of the Fornax distribution. Using the variance calculation from Leaman et al. (2013), $\text{variance} = 0.47$, brings Fornax into consistency with our sample.

Although we expect larger observational errors to at least be partly responsible for the extra broadness observed in the M31 dwarf galaxies, we do not expect them to be the sole contributors to this observed broadness. Given that our dwarfs are in general more massive than most MW dSphs with derived MDFs, we expect them to be broader in general. More massive systems are more resistant against metal-removal events such as galactic winds and are therefore able to retain their gas and continue with star formation. Less massive systems, due to their shallower potential wells, are more prone to both internally induced gas removal and externally induced gas removal such as tidal stripping. This higher efficiency of gas removal means that the SFHs of less massive systems are more easily truncated.

4.4. Radial Metallicity Profiles

In the Local Group, radial metallicity gradients are observed both photometrically and spectroscopically in many dwarf galaxies such as Sculptor (Battaglia et al. 2006), Sextans (Battaglia et al. 2011), Fornax (Tolstoy et al. 2004), Leo I (Gullieuszik et al. 2009), Leo II (Koch et al. 2007), and Draco (Kirby et al. 2011b). The presence or absence of a metallicity gradient is a clue to the star formation, chemical enrichment, and dynamical history of these objects. The details of the star-formation process, such as environmentally induced truncation or extension of star formation by gas expulsion or accretion, can also be deduced based on the radial metallicity behavior.

Examinations of radial metallicity trends for some of our galaxies (M32: Rose et al. 2005; NGC 205: Koleva et al. 2011; NGC 147 and NGC 185: Geha et al. 2010; And II: Ho et al. 2012; and And VII: Grebel & Guhathakurta 1999) have been previously presented based on either binned profiles or long-slit

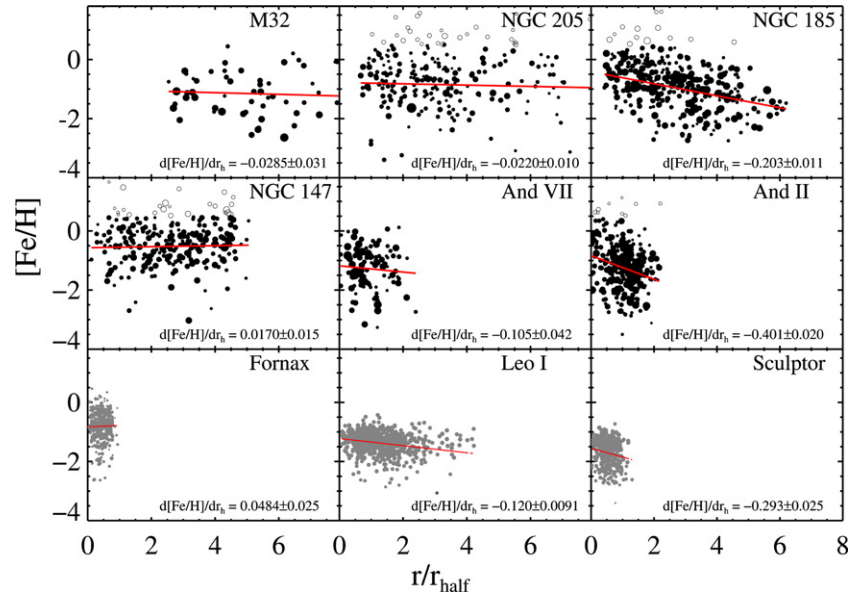


Figure 10. Radial metallicity distribution of the six sample galaxies (top two rows) and three reference MW dSphs (bottom row). Black filled circles are the M31 dwarf stars within the bounds of the C13 calibration, and unfilled circles are stars outside of the calibration regions. The individual symbol sizes are inversely correlated with their respective errors, with larger symbols representing stars with smaller errors and smaller symbols representing stars with larger errors. Overlaid as a red solid line is the best-fit line to the radial metallicity distribution of stars that lie within the bounds of the calibration (black filled circles).

spectroscopy. In Figure 10, we show the radial metallicity trends for each galaxy from its constituent RGB population. We plot the distance from the galaxy center in units of elliptical half-light radii from McConnachie (2012). Although previous works such as K11 have used the core radius as a size indicator, here we use the half-light radius because the surface-brightness profiles of our dwarf galaxies are poorly fit by King profiles. The red lines in Figure 10 are the best-fit, error-weighted, linear least-squares fit to the data. We also determine radial metallicity distributions for Fornax, Leo I, and Sculptor as a function of core radius and compared them to the Kirby et al. (2011b) distributions as a sanity check. We find excellent agreement between the K11 results and our measured radial slopes as a function of core radius. For uniformity, however, we show the radial metallicity profiles for these MW dSphs as a function of half-light radius in the bottom row of Figure 10.

As shown in Figure 10, the radial metallicity distribution for our six M31 satellites shows the same diversity as the MW satellites. Two of our galaxies, NGC 185 and And II, show significant radial gradients, with stars in the outer radii being more metal-poor than those residing in the more central radii. The slopes of M32, NGC 205, NGC 147, and And VII are all consistent with zero or nearly zero. In no case do we see a significant rise and subsequent flattening in the radial gradients in the outskirts, as was seen for Sculptor (Battaglia et al. 2008). These trends do not change significantly with the addition of stars that fall outside the C13 calibration region. In the case of NGC 185, including these stars increases the steepness of the radial gradient, and for And II, the presence of two stars in the outer regions with higher metallicities slightly decreases the gradient slope. However, because these stars are not anchored by the calibration, we do not include them in the analysis of the radial gradient slope.

Comparing our observed radial trends to previous works for each individual galaxy, we find that for four of our galaxies the trends are consistent with previously published works. For NGC 205, the radial coverage in Koleva et al. (2011) extends out to the effective radius, whereas our sample extends out to

well over five effective radii but does not cover the innermost regions because of crowding issues. Thus, while they see a radial trend in the inner regions of the galaxy, the difference in spatial coverage between our sample and theirs allows for the validity of both results. However, for NGC 185 our results are inconsistent with that of Geha et al. (2010), who observed a flat radial trend for NGC 185. The difference between our work and theirs is twofold: we utilize a different metallicity calibration and our profiles are unbinned, which avoids smoothing out the signatures of any possible gradient.

For our sample of six M31 satellites along with the three MW dSphs, we do not observe any trends in the slope of the radial gradient as a function of luminosity, distance from host, or dynamical state. Four of our galaxies, NGC 205, NGC 185, NGC 147, and And II, are rotationally supported, yet only NGC 185 and And II possess radial gradients. NGC 205 and NGC 147 are flat across five half-light radii, showing that radial coverage is not an issue and that even at large radii, the metallicity spread is similar to the inner radii. This lack of a trend between rotational support and the presence of a radial gradient is in tension with the observations of Leaman et al. (2013), who found that v/σ and the slope of the gradient are correlated for their sample, which includes LMC, Small Magellanic Cloud (SMC), Wolf–Lundmark–Mellote, Fornax, and Sculptor. If we put our dwarf galaxies on this relation, we find that our sample introduces a very large scatter in the relation, such that it is no longer statistically significant.

The radial metallicity behavior of each galaxy holds clues to the dispersion of metals during the star-formation process. Flat radial gradients can be a product of either a well-mixed interstellar medium or from tidal interactions between a dwarf satellite and its parent galaxy. Galaxy-wide mixing of gas could be due to wind-driven expulsion of gas; if a galaxy is massive enough, this gas eventually is recaptured and rains back onto the system (Mac Low & Ferrara 1999). Tidal interactions between a satellite and its parent galaxy can both disrupt stellar orbits and drive the inflow of gas into the system, resulting in additional pockets of star formation (Mayer et al.

2006). NGC 205 and NGC 147 have both been shown to be undergoing tidal disruption by M31 (Choi et al. 2002; Lewis et al. 2013; Ibata et al. 2013), which may explain their flat gradients.

Strong radial gradients, on the other hand, could be a result of purely internal evolution or external inflow of metal-rich gas. Internal evolution leading to a strong radial gradient requires that the galaxy be kinematically undisturbed and that star formation proceeds over a longer span such that metals expelled from previous generations of stellar evolution have time to gravitationally sink toward the center of the galaxy (Schroyen et al. 2013). This scenario may explain NGC 185 and And II's strong radial gradient. Although tidal interactions cannot be ruled out for these two objects, the lack of radial abundance gradients may indicate that these objects have suffered less than satellites that are fully mixed. NGC 185's SFH has been shown by Butler & Martínez-Delgado (2005) to be quite extended. McConnachie et al. (2007) showed that And II possesses an intermediate-aged population that is centrally concentrated compared to the older stellar population; the superposition of two stellar populations with different concentration indices may explain the strong gradient observed. External mechanisms leading to a metallicity gradient include inflow of metal-rich gas, but this requires that the gas be funneled directly into the central regions of the galaxy, setting off star formation. However, in order to better determine which of these mechanisms is responsible for the radial trends in these galaxies, accurate ages and stronger constraints on the SFHs of these objects are required.

5. CONCLUSION

In this paper, we present detailed metallicities of individual RGB stars within the six most luminous M31 dwarf galaxy satellites. Using a new CaT metallicity calibration, we obtained $[\text{Fe}/\text{H}]$ values from direct measurements of the CaT lines in individual RGBs. We presented the global properties, metallicity distributions, and radial metallicity profiles for these six dwarf galaxies. This sample represents the first homogeneous spectroscopic metallicity analysis of individual stars within these galaxies and, as a whole, is the most complete work on metallicity for the M31 dwarf galaxy system. We summarize our results as follows.

1. The $\langle[\text{Fe}/\text{H}]\rangle$ of these six dwarf galaxies places them on the observed $[\text{Fe}/\text{H}]$ –luminosity relation of MW and M31 satellites. Contrary to K11, we do not observe a negative trend between $\sigma([\text{Fe}/\text{H}])$ and luminosity such that more luminous galaxies have smaller $\sigma([\text{Fe}/\text{H}])$. Instead, we observe that the trend disappears with the inclusion of more luminous satellites. However, without available data for $\sigma([\text{Fe}/\text{H}])$ that cover the full spatial extent of LMC, SMC, and Sagittarius, we cannot discard the possibility that this lack of a trend is only observed for luminous M31 satellites. Future work on the metallicity of the newly discovered luminous M31 satellites (Martin et al. 2013), as well as detailed metallicity studies of fainter M31 satellites, should answer whether the metallicity dispersion trends seen in M31 are representative of all dwarf galaxies or only that of M31 satellites.
2. The observed MDFs for our dwarf galaxies are in general broader than that observed for MW dSphs, most of which are less luminous than the galaxies in our sample. Even after accounting for a larger observational error inflating the MDF of our galaxies, we still observe this enhanced

broadness for the four most luminous systems. This broadness is expected given that most of the dwarf galaxies in our sample are more massive than MW dSphs that have derived MDFs. The agreement between the leaky box model and our observed metallicity distributions, combined with the very low effective yields for most systems, shows that gas outflows played a role in the SFHs of these galaxies. However, due to the large observational errors of our sample and uncertainties, we are unable to quantify the strength of such outflows or probe additional mechanisms such as gas inflows in guiding the chemical evolution of these galaxies.

3. The radial metallicity profiles of these six dwarf galaxies show the same diversity that has been observed for MW dSphs from K11 and for other local dwarf ellipticals (Koleva et al. 2011). We do not observe any trend between galaxy luminosity, distance from host, or dynamical state and the presence of a radial gradient. Of our six galaxies, only two, NGC 185 and And II, show evidence of radial metallicity gradients. In order to determine the physical mechanisms required to produce these trends, accurate stellar ages and SFHs are required, which we leave for future works.

We thank the anonymous referee for helpful suggestions that improved this paper. M.G. acknowledges support from NSF grant AST-0908752. E.J.T. acknowledges that the support for this work was provided by NASA through Hubble Fellowship grant 51316.01 awarded by the Space Telescope Science Institute, which is operated by the Association of Universities for Research in Astronomy, Inc., for NASA, under contract NAS 5-26555.

REFERENCES

- Aaronson, M., & Mould, J. 1985, *ApJ*, **290**, 191
 Andrews, B. H., & Martini, P. 2013, *ApJ*, **765**, 140
 Aparicio, A., Carrera, R., & Martínez-Delgado, D. 2001, *AJ*, **122**, 2524
 Armandroff, T. E., & Da Costa, G. S. 1991, *AJ*, **101**, 1329
 Armandroff, T. E., & Zinn, R. 1988, *AJ*, **96**, 92
 Battaglia, G., Irwin, M., Tolstoy, E., et al. 2008, *MNRAS*, **383**, 183
 Battaglia, G., Tolstoy, E., Helmi, A., et al. 2006, *A&A*, **459**, 423
 Battaglia, G., Tolstoy, E., Helmi, A., et al. 2011, *MNRAS*, **411**, 1013
 Brown, T. M., Tumlinson, J., Geha, M., et al. 2012, *ApJL*, **753**, L21
 Buonanno, R., Corsi, C. E., Fusi Pecci, F., Hardy, E., & Zinn, R. 1985, *A&A*, **152**, 65
 Butler, D. J., & Martínez-Delgado, D. 2005, *AJ*, **129**, 2217
 Caldwell, N., Armandroff, T. E., Seitzer, P., & Da Costa, G. S. 1992, *AJ*, **103**, 840
 Carrera, R., Gallart, C., Pancino, E., & Zinn, R. 2007, *AJ*, **134**, 1298
 Carrera, R., Pancino, E., Gallart, C., & del Pino, A. 2013, *MNRAS*, **434**, 1681
 Choi, P. I., Guhathakurta, P., & Johnston, K. V. 2002, *AJ*, **124**, 310
 Coelho, P., Mendes de Oliveira, C., & Cid Fernandes, R. 2009, *MNRAS*, **396**, 624
 Cole, A. A., Smecker-Hane, T. A., Tolstoy, E., Bosler, T. L., & Gallagher, J. S. 2004, *MNRAS*, **347**, 367
 Coleman, M. G., & de Jong, J. T. A. 2008, *ApJ*, **685**, 933
 Collins, M. L. M., Chapman, S. C., Rich, R. M., et al. 2013, *ApJ*, **768**, 172
 de Boer, T. J. L., Tolstoy, E., Hill, V., et al. 2012a, *A&A*, **544**, A73
 de Boer, T. J. L., Tolstoy, E., Hill, V., et al. 2012b, *A&A*, **539**, A103
 Dekel, A., & Silk, J. 1986, *ApJ*, **303**, 39
 Dolphin, A. E., Weisz, D. R., Skillman, E. D., & Holtzman, J. A. 2005, *arXiv:astro-ph/0506430*
 Faber, S. M., & Lin, D. N. C. 1983, *ApJL*, **266**, L17
 Faber, S. M., Phillips, A. C., Kibrick, R. I., et al. 2003, *Proc. SPIE*, **4841**, 1657
 Feigelson, E. D., & Jogesh Babu, G. 2012, *Modern Statistical Methods for Astronomy* (Cambridge: Cambridge Univ. Press)
 Frebel, A., Simon, J. D., Geha, M., & Willman, B. 2010, *ApJ*, **708**, 560
 Gallart, C., Freedman, W. L., Aparicio, A., Bertelli, G., & Chiosi, C. 1999, *AJ*, **118**, 2245
 Geha, M., Guhathakurta, P., Rich, R. M., & Cooper, M. C. 2006, *AJ*, **131**, 332
 Geha, M., van der Marel, R. P., Guhathakurta, P., et al. 2010, *ApJ*, **711**, 361

- Gilmore, G., Norris, J. E., Monaco, L., et al. 2013, *ApJ*, **763**, 61
- Girardi, L., Bertelli, G., Bressan, A., et al. 2002, *A&A*, **391**, 195
- Gnedin, O. Y., Hernquist, L., & Ostriker, J. P. 1999, *ApJ*, **514**, 109
- Gray, D. F. 2005, *The Observation and Analysis of Stellar Photospheres* (Cambridge: Cambridge Univ. Press)
- Grcevich, J., & Putman, M. E. 2009, *ApJ*, **696**, 385
- Grebel, E. K., & Guhathakurta, P. 1999, *ApJL*, **511**, L101
- Grillmair, C. J., Lauer, T. R., Worthey, G., et al. 1996, *AJ*, **112**, 1975
- Gullieuszik, M., Held, E. V., Rizzi, L., et al. 2007, *A&A*, **467**, 1025
- Gullieuszik, M., Held, E. V., Saviane, I., & Rizzi, L. 2009, *A&A*, **500**, 735
- Gunn, J. E., & Gott, J. R., III 1972, *ApJ*, **176**, 1
- Helmi, A., Irwin, M. J., Tolstoy, E., et al. 2006, *ApJL*, **651**, L121
- Ho, N., Geha, M., Munoz, R. R., et al. 2012, *ApJ*, **758**, 124
- Holtzman, J. A., Afonso, C., & Dolphin, A. 2006, *ApJS*, **166**, 534
- Howley, K. M., Guhathakurta, P., van der Marel, R., et al. 2013, *ApJ*, **765**, 65
- Ibata, R. A., Lewis, G. F., McConnachie, A. W., et al. 2013, *ApJ*, **765**, 15
- Kalirai, J. S., Beaton, R. L., Geha, M. C., et al. 2010, *ApJ*, **711**, 671
- Kirby, E. N., Cohen, J. G., Smith, G. H., et al. 2011a, *ApJ*, **727**, 79
- Kirby, E. N., Guhathakurta, P., Bolte, M., Sneden, C., & Geha, M. C. 2009, *ApJ*, **705**, 328
- Kirby, E. N., Guhathakurta, P., & Sneden, C. 2008a, *ApJ*, **682**, 1217
- Kirby, E. N., Lanfranchi, G. A., Simon, J. D., Cohen, J. G., & Guhathakurta, P. 2011b, *ApJ*, **727**, 78
- Kirby, E. N., Simon, J. D., Geha, M., Guhathakurta, P., & Frebel, A. 2008b, *ApJL*, **685**, L43
- Kobayashi, C., Umeda, H., Nomoto, K., Tominaga, N., & Ohkubo, T. 2006, *ApJ*, **653**, 1145
- Koch, A., Grebel, E. K., Kleyna, J. T., et al. 2007, *AJ*, **133**, 270
- Koch, A., Grebel, E. K., Wyse, R. F. G., et al. 2006, *AJ*, **131**, 895
- Koleva, M., Prugniel, P., de Rijcke, S., & Zeilinger, W. W. 2011, *MNRAS*, **417**, 1643
- Lanfranchi, G. A., & Matteucci, F. 2004, *MNRAS*, **351**, 1338
- Larson, R. B. 1974, *MNRAS*, **169**, 229
- Leaman, R., Venn, K. A., Brooks, A. M., et al. 2013, *ApJ*, **767**, 131
- Lewis, G. F., Braun, R., McConnachie, A. W., et al. 2013, *ApJ*, **763**, 4
- Lokas, E. L., Kazantzidis, S., Klimontowski, J., Mayer, L., & Callegari, S. 2010, *ApJ*, **708**, 1032
- Lynden-Bell, D. 1975, *VA*, **19**, 299
- Mac Low, M.-M., & Ferrara, A. 1999, *ApJ*, **513**, 142
- Maeder, A. 1992, *A&A*, **264**, 105
- Martin, N. F., Slater, C. T., Schlafly, E. F., et al. 2013, *ApJ*, **772**, 15
- Matteucci, F. (ed.) 2001, *The Chemical Evolution of the Galaxy* (Astrophysics and Space Science Library, Vol. 253; Dordrecht: Kluwer), 293
- Mayer, L., Mastropietro, C., Wadsley, J., Stadel, J., & Moore, B. 2006, *MNRAS*, **369**, 1021
- McConnachie, A. W. 2012, *AJ*, **144**, 4
- McConnachie, A. W., Arimoto, N., & Irwin, M. 2007, *MNRAS*, **379**, 379
- McConnachie, A. W., Irwin, M. J., Ferguson, A. M. N., et al. 2005, *MNRAS*, **356**, 979
- Monachesi, A., Trager, S. C., Lauer, T. R., et al. 2011, *ApJ*, **727**, 55
- Olszewski, E. W., Schommer, R. A., Suntzeff, N. B., & Harris, H. C. 1991, *AJ*, **101**, 515
- Ostheimer, J. C., Jr. 2003, PhD thesis, Univ. Virginia
- Piatek, S., & Pryor, C. 1995, *AJ*, **109**, 1071
- Pont, F., Zinn, R., Gallart, C., Hardy, E., & Winnick, R. 2004, *AJ*, **127**, 840
- Prantzos, N., & Silk, J. 1998, *ApJ*, **507**, 229
- Reitzel, D. B., & Guhathakurta, P. 2002, *AJ*, **124**, 234
- Rose, J. A., Arimoto, N., Caldwell, N., et al. 2005, *AJ*, **129**, 712
- Rutledge, G. A., Hesser, J. E., Stetson, P. B., et al. 1997, *PASP*, **109**, 883
- Saviane, I., da Costa, G. S., Held, E. V., et al. 2012, *A&A*, **540**, A27
- Schroyen, J., De Rijcke, S., Koleva, M., Cloet-Osselaer, A., & Vandenbroucke, B. 2013, *MNRAS*, **434**, 888
- Shetrone, M., Venn, K. A., Tolstoy, E., et al. 2003, *AJ*, **125**, 684
- Simon, J. D., & Geha, M. 2007, *ApJ*, **670**, 313
- Simon, J. D., Geha, M., Minor, Q. E., et al. 2011, *ApJ*, **733**, 46
- Skillman, E. D., Kennicutt, R. C., & Hodge, P. W. 1989, *ApJ*, **347**, 875
- Smecker-Hane, T. A., Stetson, P. B., Hesser, J. E., & Lehnert, M. D. 1994, *AJ*, **108**, 507
- Starkenbourg, E., Hill, V., Tolstoy, E., et al. 2010, *A&A*, **513**, A34
- Stetson, P. B., Hesser, J. E., & Smecker-Hane, T. A. 1998, *PASP*, **110**, 533
- Tinsley, B. M. 1980, *FCP*, **5**, 287
- Tollerud, E. J., Beaton, R. L., Geha, M. C., et al. 2012, *ApJ*, **752**, 45
- Tolstoy, E., Hill, V., & Tosi, M. 2009, *ARA&A*, **47**, 371
- Tolstoy, E., Irwin, M. J., Cole, A. A., et al. 2001, *MNRAS*, **327**, 918
- Tolstoy, E., Irwin, M. J., Helmi, A., et al. 2004, *ApJL*, **617**, L119
- Tremonti, C. A., Heckman, T. M., Kauffmann, G., et al. 2004, *ApJ*, **613**, 898
- Vargas, L. C., Geha, M. C., & Tollerud, E. J. 2014, *ApJ*, **790**, 73
- Walker, M. G., Mateo, M., Olszewski, E. W., et al. 2007, *ApJL*, **667**, L53
- Watkins, L. L., Evans, N. W., & An, J. H. 2010, *MNRAS*, **406**, 264
- Willman, B., Geha, M., Strader, J., et al. 2011, *AJ*, **142**, 128
- Winnick, R. A. 2003, PhD thesis, Yale Univ.
- Yniguez, B., Garrison-Kimmel, S., Boylan-Kolchin, M., & Bullock, J. S. 2013, *MNRAS*, **439**, 73
- Zinn, R., & West, M. J. 1984, *ApJS*, **55**, 45